OXFORD UNIVERSITY PRESS | Microscopy

Detection of Local Chemical States of Lithium and their Spatial Mapping by Scanning Transmission Electron Microscopy, Electron Energy-Loss Spectroscopy, and Hyperspectral Image Analysis

Journal:	*Microscopy*
Manuscript ID	MICRO-2016-00044.R1
Manuscript Type:	Invited Special Issue
Date Submitted by the Author:	n/a
Complete List of Authors:	Muto, Shunsuke; Nagoya University, Institute of Materials and Systems for Sustainability Tatsumi, Kazuyoshi; Nagoya University, Institute of Materials and Systems for Sustainability
Key Words:	spectral image, lithium ion battery, cathode active materials, non-negative matrix factorization, multivariate curve resolution, first principles calculation

Detection of Local Chemical States of Lithium and their Spatial Mapping by Scanning Transmission Electron Microscopy, Electron Energy-Loss Spectroscopy, and Hyperspectral Image Analysis

Shunsuke Muto and Kazuyoshi Tatsumi

Advanced Measurement Technology Center, Institute of Materials and Systems for Sustainability, Nagoya University, Chikusa-ku, Nagoya 464-8603, Japan

Corresponding author: S. Muto

Phone: +81 52 789 5200

Fax: +81 52 789 5137

E-mail: smuto@imass.nagoya-u.ac.jp

Keywords: spectral image, lithium ion battery, cathode active materials, non-negative matrix factorization, multivariate curve resolution, first principles calculation

Running title: *STEM-Hyperspectral image analysis of Li*

Total no. of pages: 26

No. of figures: 9

ABSTRACT

Advancements in the field of renewable energy resources have led to a growing demand for the analysis of light elements at the nanometer scale. Detection of lithium is one of the key issues to be resolved for providing guiding principles for the synthesis of cathode active materials, and degradation analysis after repeated use of those materials. We have reviewed the different techniques currently used for the characterization of light elements such as high resolution transmission electron microscopy, scanning transmission electron microscopy (STEM), and electron energy-loss spectroscopy (EELS). In the present study, we have introduced a methodology to detect lithium in solid materials, particularly for cathode active materials used in lithium ion battery. The chemical states of lithium were isolated and analyzed from the overlapping multiple spectral profiles, using a suite of STEM, EELS and hyperspectral image analysis. The method was successfully applied in the chemical state analyses of hetero-phases near the surface and grain boundary regions of the active material particles formed by chemical reactions between the electrolyte and the active materials.

INTRODUCTION

Detection and quantification of light elements such as hydrogen and lithium, both of which are important for the research and development of next generation energy storage/production related materials, have long been an issue in microanalysis by electron microscopy. Although there are a number of techniques for detecting/quantifying the light elements, microscopic techniques, particularly those attached to transmission electron microscopy (TEM) are widely exploited due to their atomic-scale spatial resolution. One of the most popular analytical techniques associated with electron microscopy is energy-dispersive X-ray (EDX) spectroscopy. The conventional EDX instrument cannot detect elements lighter than boron, because of the strong absorption of these elements by the surface layers and the surrounding heavier elements, and the typical use of the beryllium window. In exceptional cases, a specially customized windowless EDX detector can detect lithium [1]. Wavelength-dispersive X-ray spectroscopy with reflection geometry has been successful in lithium detection and its chemical analysis [2]. However, the light elements yield Auger electrons as a dominant relaxation process rather than the characteristic X-rays, after the excitation of the core-electrons [3], which make detection of X-ray fluorescence from light elements even more difficult.

High-resolution transmission electron microscopy (HR-TEM) and scanning TEM (STEM) techniques, particularly with the recent development of the aberration correction technology have opened up the possibility for direct observation of lithium [4-6]. Nevertheless, their applications are limited to thin materials with high crystallinity, oriented precisely with a low-order zone axis parallel to the direction of the incident beam. Apart from the detection and quantification of lithium, it is important to probe the

different chemical states of the metal over a wide area in the form of spatial distribution maps on the nanometer scale, which is not possible by HR-S/TEM.

A promising alternative is electron energy-loss spectroscopy (EELS) attached to TEM. It probes the local chemical bonding environments of specific elements and is particularly effective for light elements [7]. For the research and development of energy storage devices such as lithium-ion batteries (LIB), it is crucial to investigate the chemical states of lithium in localized regions. This is because the performance of the battery strongly depends on the reversible extraction/insertion processes of lithium ions from the surface of the electrode material during the charge-discharge cycles. In addition, by scanning the focused electron beam down to a sub-nanometer size over the entire region of interest, it is possible to visualize the spatial distributions of lithium and its electronic states; this technique is known as STEM-EELS spectral imaging (SI) [8]. However, in the case of promising active materials for positive electrodes such as, LiM_2O_4 (spinel), $LiMO_2$ (layered rock-salt) and $LiMPO_4$ (olivine) (M = Mn, Fe, Ni, Co), the transition metal $M_{2,3}$ edges (TM 3p $\rightarrow$ 3d*) and the Li K edge (Li 1s $\rightarrow$ 2p*) have very similar energy loss values. Therefore, it is not possible to extract information about lithium from the spectra merely by selecting the lithium absorption edge with an energy slit. Kikkawa et al. determined the lithium distributions in $Li_{1.2}Mn_{0.4}Fe_{0.4}O_2$ particles by taking the second derivative of each spectrum to separate the primary sharp peak of Li–K energy-loss near-edge structure (ELNES) spectrum from the overlapping $M_{2,3}$ edges of the transition metals [9]. However, this method cannot be used to intensively investigate the chemical states of lithium and other elements since it does not allow the extraction of the entire fine structures of the spectra.

In the present review, we focus on the analysis of the chemical states of lithium

using S/TEM-EELS in combination with the hyperspectral image analysis. The spectral image data were used for the detailed chemical analysis of lithium by isolating the entire profiles of the overlapping component spectra. As an example, the application of the method to LIB cathode active materials has been presented.

METHODS

Experimental techniques for the detection of lithium by S/TEM-EELS

There are a number of ways to construct an SI dataset in S/TEM-EELS, and each method has its advantages and drawbacks [8]. Once a data cube is obtained, the same mathematical procedure can be applied regardless of the method used.

STEM-EELS-SI

The STEM-EELS-SI scheme is shown in Fig. 1(a). This method allows us to flexibly select the spatial/spectral resolution by appropriately setting the probe-size, the scan step width, and the detector dispersion. The anticipated spatial and energy drifts can be compensated in the latest commercial spectrometers using the optional functions in the controlling software platform. The spatial drift is unavoidable in the case of prolonged data collection time while scanning larger areas. The energy drift correction can be performed as a post-acquisition process because the zero-loss peak (ZLP) can be included while recording the spectral range of Li K spectrum. As a drawback, the focusing of the high density electron beam may modify or deteriorate the sample. Microscopists must pay attention to this aspect and optimize the accelerating voltage of the microscope, the probe size, the beam current and the duration required for a single acquisition in order to avoid damage to the sample. Cathode active materials tend to be

relatively radiation resistant when optimum conditions are used, whereas, anode materials and electrolytes are usually very sensitive to the high energy electron beam. In such cases, specimen cooling is often very effective.

EF-TEM-SI

Energy-filtered TEM is another method for detection of lithium, and is schematically shown in Fig. 1(b). However, in practice, this option is not always suitable for visualizing lithium distribution because the higher-order plasmon peak may overlie the onset of the Li K-edge, in which case, an appropriate pre-edge subtraction scheme can fail in the three-window EF method. The energy resolution is limited by the slit width of the energy filter used, which is usually set to a lower limit of 1 eV. For detectors with the specification of ultra-high resolution, the slit width may be as small as 0.1 eV [10]. The spatial resolution can be determined by the image magnification and the effective detector pixel number. EF-TEM allows the use of a defocused beam and may be effective for radiation-sensitive materials.

SR-EELS-SI

The third option for detecting lithium in radiation-sensitive materials utilizes the one-dimensional chemical information such as the relative chemical shift and/or spectral profile variation as a function of the distance normal to the surface/interface at the cross section of a layered sample. This method is called spatially resolved EELS (SR-EELS) which takes advantage of the position-sensitive detector based on a charge coupled device (CCD) [11,12]. The experimental setup of SR-EELS is schematically shown in Fig. 1(c). The sample is set so that the dispersion direction of the detector is parallel to

the interface. Further, each row in the 2D CCD image data corresponds to an EEL spectrum from the layer of the corresponding vertical coordinate in the sample included in the rectangular aperture, averaged over the lateral dimension of the aperture. The vertical resolution depends on the image magnification and the area of CCD used for the spectral recording. SR-EELS technique was recently applied to an all-solid-state LIB [13] for visualizing the lithium content profile near the electrolyte/electrode interface.

Hyperspectral image analysis: Why is it necessary?

Figure 2 shows the ELNES spectra of LiF and representative 3d transition metal (TM: Mn, Fe, Co, Ni) oxides located around the energy loss range of 50-80 eV. As mentioned in the Introduction, the $M_{2,3}$ spectra of TM are located at very similar energy ranges and could possibly conceal a part of the fine structure of Li K ELNES. Another difficulty in EELS analysis of lithium is the pre-edge background subtraction in thicker samples, because the third order plasmon peak (around 50-70 eV) could be overlaid near the energy-loss range. It is thus advisable to set the sample thickness to a value less than 0.4λ, where λ is the mean free path corresponding to the scattering cross-section for plasmon excitation, even though the Fourier-log deconvolution [7] is applied to obtain a single scattered spectrum. However, a small hump could not be completely removed even after pre-processing, as will be shown in the later sections. The ELNES spectra of this region obtained from several representative lithium compounds and LIB cathode materials are shown in Fig. 3. It is well recognized from the ELNES spectra of Li_2O and LiF that the fine structural signatures vary significantly depending on the chemical state of lithium. However, it is not easy to distinguish the Li K ELNES spectrum from the overlapping spectra of lithium and/or the transition metals involved.

Irrespective of using the finger printing method or first principles theoretical spectral prediction, it is necessary to isolate the Li K ELNES spectrum from the overlapping spectral profiles for interpreting the chemical states of lithium.

An indirect method to identify the chemical states of lithium is to examine the chemical states of the elements chemically bonded to lithium. In ionic ceramics such as, oxides, fluorides, and cathode active materials for LIB, the chemical changes of the other constituent elements such as transition metal elements can be used to determine the chemical state of lithium through the local electrical neutrality condition. Although it is not possible to directly analyze the lithium spectrum, the corresponding change in the chemical state can be detected from the spectra of the anions bonded to lithium, the corresponding valence changes of the transition metals, and the fine structures of the oxygen spectra [13,14,15]. However, the different spectral profiles may get overlapped when the regions exhibiting different chemical states are spatially overlapped, and spectral isolation again becomes necessary [14,15].

In order to solve the above problem, hyperspectral image analysis has been applied [16]: the spectral intensity in the collected STEM-SI or EF-TEM-SI data is a function of the two-dimensional position (x, y) on the sample and the absorption energy E, expressed in a three-dimensional matrix form (data cube), $\boldsymbol{D}(x, y, E)$. A number of attempts to statistically extract a few basis spectra and their contributions at individual positions have been reported, with the assumption that the spectral intensity, $\mathbf{S}_i(E)$ at each sample pixel is represented by a linear combination of the basis spectra, $\mathbf{s}_k(E)$ associated with the underlying chemical states or phases. Fig. 4(a) represents

$$\mathbf{S}_i(E_j; j = 1,2,..,N_{ch}) = \sum_k^K c_{i,k}\mathbf{s}_k(E_j; j = 1,2,..,N_{ch}),\ i = 1, 2, \ldots, N_{xy} \qquad (1)$$

For the convenience of mathematical manipulation, a data cube is often transformed to a two-dimensional $N_{xy} \times N_{ch}$ matrix $\boldsymbol{X}$, where $N_{xy} = N_x \times N_y$ is the number of pixels, i.e., the number of scanning steps N_x (N_y) along the x (y) direction, and N_{ch} is the number of EELS detector channels used for the analysis. In this case, the experimental spectrum at position (x, y) is stored in a row of matrix $\boldsymbol{X}$. In the case of SR-EELS data, the raw data in the two-dimensional form can be recognized as $\boldsymbol{X}$ as such. The original data matrix $\boldsymbol{X}$ can then be approximated by the matrix product of $\boldsymbol{C}$ and $\boldsymbol{S}$ in the following form (Fig. 4(b)):

$$\mathbf{X} \approx \mathbf{S}\boldsymbol{C}^{\mathrm{T}}, \text{ or } \mathbf{X} = \mathbf{S}\mathbf{C}^{\mathrm{T}} + \mathbf{E}, \quad (2)$$

where, $\mathbf{E}$ denotes the $N_{xy} \times N_{ch}$ matrix for which the entry must be the statistical error involved at each pixel in the experimental data. The superscript T denotes the transpose. Each column vector of $\boldsymbol{S}$ (referred to as 'loading' in terms of multivariate analysis) is a basis spectrum; each column vector of $\boldsymbol{C}$ (referred to as 'score') is the relative fraction of a chemical state or phase (referred to as 'component') in the region of interest, and each entry of the column vector of $\boldsymbol{C}$ represents the contribution of the loading vectors at one sampling position. When K essential spectra exist in the experimental data, then the basis spectra and the concentration coefficients can be stored in the $N_{xy} \times K$ matrix $\boldsymbol{C}$ and the $N_{ch} \times K$ matrix $\boldsymbol{S}$, respectively. The spatial distribution of the i-th spectral component can then be reconstructed by selecting the i-th column of $\boldsymbol{C}$ and rearranging the elements back to the original two-dimensional order, as shown in Fig. 4(b).

There are a number of statistical approaches to determine a solution for Eq. (1) using only the data matrix $\boldsymbol{X}$, which includes a large number of elements with a relatively small number of K. A statistical approach is expected to extract plausible $\boldsymbol{C}$

and ***S*** with much higher signal-to-noise ratios (SNRs) than for those picked up from the small number of representative sampling points in a conventional manner (i.e., point-to-point analysis). Among the various statistical approaches to solve Eq. (1) and obtain the unknown ***C*** and ***S***, principal component analysis (PCA) [17-19] is one of the most fundamental and popular methods. PCA successively casts mutually orthogonal eigenvectors (basis vectors) and the associated score images (spatial distributions of the corresponding basis vectors) in the order of significance, i.e., in the order of the magnitude of the eigenvalues through the singular value decomposition of ***X***. PCA assumes that each pixel contains a linear combination of the principal components satisfying the orthogonality condition, which usually provides physically meaningless spectral profiles.

Our research group has applied an alternative method of non-negative matrix factorization (NMF), or multivariate curve resolution (MCR), to solve Eq. (1) for the analysis of EELS-SI [14,16]. This approach was followed because NMF naturally restricts the score images and the basis spectra from being non-negative. On the other hand, the methods based on PCA allow the images and spectra to accept negative values, which hamper the direct physical interpretation of the resolved spectral profiles. We adopted the modified alternating least-square (MALS) fitting algorithm [20] to solve a number of problems such as the mapping of different phases in the degradation of the LIB cathodes [14,15] and the chemical states of nitrogen in nitrogen-doped TiO_2 [21]. In the NMF scheme, C_{ik} denotes the relative composition of the k-th component spectrum (k-th column of **S**) at the i-th spatial coordination if the energy range covers a single elemental spectrum and the spectral intensities are normalized by the area subtended by each component spectrum [16].

Non-negative matrix factorization with ALS is performed by simply minimizing the squared error, $\|\boldsymbol{X} - \boldsymbol{S}\boldsymbol{C}^{\mathrm{T}}\|^2$, which is the Euclidean distance between the experimental and the reconstructed data. The basic idea of the ALS procedure is very simple and the core algorithm is described as follows [20]:

C = rand(N_{xy},K); %initialize **C** as random dense matrix

for i=1:maxiter

Solve for **S** in matrix equation $\mathbf{S}\mathbf{C}^{\mathrm{T}}\mathbf{C} = \mathbf{X}\mathbf{C}$.

Set all negative elements in **S** to 0.

Solve for **C** in matrix equation $\mathbf{S}^{\mathrm{T}}\mathbf{S}\mathbf{C}^{\mathrm{T}} = \mathbf{S}^{\mathrm{T}}\mathbf{X}$.

Set all negative elements in **C** to 0.

End

Here, maxiter is the number of iterations. The set of matrix equations in the for-end loop is equivalent to the least-square fit and derives a set of compromise solutions for the matrices **C** and **S**. In order to guarantee that the entries in **C** and **S** are non-negative, all the negative entries are replaced by zero and the recursive arithmetic is repeated until the matrices are eventually converged to the solution when all the entries are non-zero.

There are two serious and intrinsic difficulties in the conventional NMF method. First, the optimization algorithm does not always converge to the optimal $\boldsymbol{C}$ and $\boldsymbol{S}$, because the optimization problem has multiple local minima (non-convex). Hence, the best solution must be empirically selected by repeated optimizations of $\boldsymbol{S}$ and $\boldsymbol{C}$ from different initial configurations. Second, NMF sets the number of the spectral components in advance. The NMF technique was conventionally applied to the datasets

for resolving the spectral components by increasing the number of components until the spatial distribution of the residual component exhibits only statistical noise showing no significant texture that correlates with the microstructure. Furthermore, the original NMF-ALS or MALS procedure performed under certain conditions can yield a solution of a major component spectrum and a difference spectrum between the major and the minor components only if one of the pure components extends over a broader range than the other [22]. Such a situation can occur when the minor component spectrum does not oscillate with large amplitudes and the spectral components are not spatially isolated. This difficulty is partially overcome by using a more recent NMF algorithm [23], which has been applied to the examples studied in the present work. A detailed description of the algorithms can be found in the literature [16,20,23,24].

Recently [24], we have proposed a new NMF method which can mostly overcome the problems discussed above by imposing: i) a sparse penalty to optimize the number of components, called automatic relevance determination [25], and ii) a spatial orthogonal constraint on **C** [26]. The proposed schemes can successfully resolve the physically meaningful components by reducing the search space for low rank matrices, even in cases when the conventional NMF is unable to resolve the components correctly.

RESULTS

We demonstrate here, several successful application examples wherein the NMF method was used for the analysis of a promising cathode active material, $LiNi_{0.8}Co_{0.15}Al_{0.05}O_2$ (NCA) in LIBs [22,27].

Sample preparation

$LiNi_{0.8}Co_{0.15}Al_{0.05}O_2$ powder was synthesized by a standard co-precipitation method. The positive electrodes were fabricated from NCA active material particles, conductive carbon, and polyvinylidene difluoride binder. The positive electrodes were assembled into cylindrical cells with negative electrodes of graphite and 1 M $LiPF_6$-EC/DEC electrolyte solution. After a few initial charge/discharge cycles, the cell was discharged to 3.0 V and then disassembled. The positive electrode was collected and washed in DEC to remove any residual electrolyte solution. The sample for TEM analysis was prepared by focused ion beam thinning to produce a thin film (~100 nm thick) of area ~10 μm^2, which is equivalent to the area of a secondary particle. The samples prepared by the above-mentioned procedure were procured from Toyota Central R&D Laboratories Inc [14,22,27].

SI data were acquired at room temperature using a Jeol JEM2100 S/TEM equipped with a Gatan Enfina 1000 spectrometer, with a probe size of 1-2 nm, a typical acquisition time of 0.8 s, and a scan step of 10-30 nm. The energy dispersion was set to 0.1 eV/channel and the energy loss range was set from −10 to 120 eV including the zero loss peak. The collected spectra were aligned so that the ZLPs were located at the zero energy position. They were then deconvolved by the Fourier-log method [7] to remove the ZLPs and the multiple loss components. The Li K, Co, and Ni $M_{2,3}$ ELNES spectra start at around 58−65 eV so that they lie on the high-energy tail of the volume plasmon peak. The spectra were then carefully isolated by subtracting the pre-edge background using a power law and selecting an appropriate pre-edge region to extract the core-loss spectra in the energy range of 56−80 eV. It has to be mentioned that a small blunt pre-edge peak is also observed in the spectra of lithium-3d transition metal oxides,

which corresponds to the transition to the 3d empty states of the transition metals. This peak is not considered in the present study.

Theoretical prediction of spectral profiles

In order to clarify the origin of the extracted unknown spectral profiles, we compared them with the theoretical Li–K ELNES spectra of several conceivable candidates among the compounds of lithium. This was performed using the augmented plane wave + local orbital (APW+lo) method within the generalized gradient approximation in WIEN2k code [28] in order to compare the relative peak intensities and the positions. The axis for the energy loss was calibrated using the experimental and theoretical spectra of Li_2O and $LiNiO_2$. We did not take the Co– and Ni–$M_{2,3}$ ELNES spectra into consideration in the calculation. This was because the characteristic peaks extracted in the energy range of 55-65 eV had to be derived solely from the Li–K ELNES spectrum due to the delayed maxima of Co– and Ni–$M_{2,3}$ ELNES. It should be noted that, in the case of the Li–K ELNES spectrum for which transitions from the shallow core states are studied, theoretical predictions based on the density functional theory generally do not always reproduce the experimental spectra well, particularly the peak separation and the relative peak intensities. A recent theoretical approach that involves solving the electron/core–hole Bethe–Salpeter equation (BSE) partly improves the situation [29]. However, the BSE scheme cannot be applied to complex structures such as the one in the present case due to its very high computational cost. The discrepancy between the theoretical and the experimental spectra is not due to the

disregard to the transition metals; rather, it is ascribed to the limitations of the discrete Fourier transform scheme. The axis for the energy loss in the theoretical spectra was calibrated so that the position of the first distinct peak of $LiNiO_2$ matches the experimental one.

Formation of hetero-phase at the surface by reaction with electrolyte

Figure 5(a) shows the annular dark-field (ADF) STEM image of a secondary particle of the active material (before the cycling tests). This particle is an agglomeration of small primary particles with random orientations. The grains that satisfy the conditions for strong Bragg reflection have bright contrasts. SI was conducted in the region inside the red broken-line frame in Fig. 5(a), where the number of sampling points was 300 x 300 pixels^2 with an interval of 10 nm. The extracted core-loss spectrum from the entire region after subtracting the pre-edge background is shown in Fig. 5(b). The expected energy values for the onset of Li–K, Co–$M_{2,3}$, and Ni–$M_{2,3}$ ELNES are indicated in Fig. 5(b). Since the latter two exhibited delayed maxima, the sharp peak at ~62 eV is expected to belong to Li–K ELNES. All the other features are contained in the broad peak appearing at 63–75 eV.

We first attempted to obtain an energy-filtered image by selecting the first distinct peak around 62 eV, and the result is shown in Fig. 5(c). The surface regions and grain boundaries appear bright, which apparently suggests lithium enrichment around the regions. For a detailed examination, EEL spectra were extracted from the two positions marked in Fig. 5(a), and are displayed in Fig. 5(d). In contrast to the EELS spectrum from spot #1, that from spot #2 showed a sharp peak at ~60 eV with a significantly higher intensity than the broad peak on the high energy side. This implies that different

compositions and/or chemical states are present in the boundary areas, rather than the lithium enrichment in the in-grain regions. Furthermore, a small feature was observed at 57-58 eV indicated by an arrow in Fig. 5(d), which may be attributed to statistical noise.

Figures 6(a) and (b) show the spatial distributions of the resolved components, assuming that there are two components. The corresponding spectral profiles of the pure components are shown in Fig. 6(c). Since NMF assumes that the spectral profile at each position is a linear combination of the spectra of the pure components, it can extract the underlying components only when the weight (composition) of each component spectrum changes independently with the spatial position. Bearing this in mind and inspecting the resolved components and their spatial distributions in Figs. 6(a) and (b), component #1 can be assigned to the same component in Fig. 5(b) (i.e., the same spectrum from spot #1 shown in Fig. 5(d)); this component is always isolated as the main component. Specifically, it is an inseparable combination of the spectra of Li–K, Co–$M_{2,3}$ and Ni–$M_{2,3}$ corresponding to the initial NCA phase of uniform composition. Component #2 is considered to be a Li-related phase with a different chemical state. We confirmed the uniqueness of the spectral decomposition by applying NMF to another secondary particle and identical spectral profiles were obtained for components #1 and #2 with similar spatial distributions.

The main sharp peak of component #2 around 62 eV is shifted to the high energy side relative to that of component #1; this peak and the pre-peak around 58 eV are not clearly visible using the point-to-point analysis (see Fig. 5(d)), but it becomes visible after applying NMF and extracting the statistical tendencies from many sampling points. This is attributed to the overlap of the multiple states within the sample thickness in the projected direction and the low SNR obtained from a single spot.

On the other hand, we previously reported [14] that fluorine was found on the surfaces of primary particles, presumably because chemical reactions during the charge–discharge cycles occur at the surface regions that are in contact with the $LiPF_6$ electrolyte. The thickness of the fluorine-containing surface regions corresponds well to that of component #2. A small amount (i.e., a few atomic percent) of phosphorus was also found in the same regions as fluorine (not shown). Thus, the possible candidate for component #2 is LiF, which is produced by the decomposition or reaction of the electrolyte, as reported recently [30].

In order to elucidate the origin of component #2, we compared the spectrum with the theoretical Li–K ELNES spectra of several conceivable candidates among the Li compounds. Since the experimental Li–K ELNES spectra from Li–P–F derivatives are not available, we calculated the theoretical spectra for $LiNiO_2$, LiF, $LiPF_6$, and other possible compounds [30]. Of the theoretically predicted spectra, the positions of the two characteristic peaks best agree with those of $Li_xPO_yF_z$-type materials group (i.e., based on the $LiPF_6$ structure; x, y, z are adjustable parameters to ensure electrical neutrality), which was suggested as an electrolyte derivative [30]. Other conceivable chemical states of lithium such as Li occupying the Ni site, Li replacing Ni in the rock-salt type phase and LiF phase can be readily excluded as possible candidates based on the significant discrepancies in the spectral profile. The experimentally observed chemical shifts of the main peak and the pre-peak (see Fig. 6(c)) can be derived from the local atomic configurations (Li and its six nearest neighbor atoms) of LiO_4F_2 and LiF_6 clusters, as shown in Fig. 7. This result is consistent with a recent surface analysis by X-ray photoelectron spectroscopy [31]. The present method revealed that the product phase is distributed not only over the surface of the secondary particles but also along the grain

boundaries between the primary particles of the active material. Since the unstable residual $LiPF_6$ may decompose and become partially oxidized, component #2 in Fig. 6(c) may be due to a mixture of different combinations of y and z that form LiO_iF_{6-i}-type local configurations rather than a single phase.

Formation of degradation layer after cycling at elevated temperatures

It is well established that in NCA cathode active material particles, the NiO-like degraded phase grows near the surface and the grain boundaries after 500 cycles at 70 ºC, as observed in the same material cycled at 80 ºC [14]. We estimated the relative amounts of the NiO-like phase before and after cycling at 70 and 80 ºC, which mostly explained the fading capacity of the positive electrode [22]. In accordance with the results above, it was shown that some Li atoms substitute Ni atoms in the NiO-like degraded phase. This was confirmed by examining the sample after 500 cycles at 70 ºC.

The SI data cube sampled from a 40 x 100 $pixel^2$ area and the low-loss region covering the Li-K, Co-$M_{2,3}$ and Ni-$M_{2,3}$ edges were again treated by the NMF technique. The ADF-STEM image, and the spatial distribution maps of the extracted spectral components are respectively shown in Figs. 8(a), (b) and (c). The figures indicate the results obtained by 2-component analyses, in which the uniform background components were omitted. The extracted spectral profiles are shown in Fig. 8(d). Component #1 (black line) corresponds to the original $LiNiO_2$-based phase, as shown in the previous section. Component #2 (red line) shown in Fig. 8(d) was newly found in the cycled sample. This component was always found in the analyzed particles and its spatial distributions correlated well with those of the NiO-like phase in the same area. The present new phase and the NiO-like phase are distributed near the surfaces in the

particle grains, whereas lithium fluorophosphates are found in the initial state along the peripheries of the particle surfaces [27]. This suggests that component #2 could be interpreted as Li occupying a Ni site in the NiO structure. The point-to-point EELS analysis in our previous study [32] confirmed that Li is actually present in the NiO-like phase.

The theoretical Li-K ELNES spectra for the substitution of a Li atom at the Ni site and the pristine $LiNiO_2$ phase are shown in Fig. 9. As has been mentioned above, theoretical predictions based on the discrete functional theory do not generally reproduce the experimental spectra well with respect to the peak separation and the relative peak intensities [29]. However, Fig. 9 actually shows that the theoretical spectrum of Li in NiO (red line) corresponds quite well with the solution of component #2 obtained by NMF (Fig. 8(d)).

CONCLUDING REMARKS

In this article, we have demonstrated the detection and analysis of lithium and its chemical states in solid materials using a suite of STEM-EELS spectral image data and hyperspectral image analysis. The present methodology is applicable not only to lithium analysis by STEM-EELS but also a wide variety of general spectral image datasets such as STEM-EDX, Fourier transform infrared spectroscopy and time of flight secondary ion mass spectroscopy.

It should be noted that the hyperspectral image analysis presented here does not merely visualize hidden information from datasets with low SNR; it casts a robust and trustable technique for efficiently extracting the complete significant information included in the huge dataset obtained from automated spectral measurements carried out

by PC-controlled analytical instruments. The present multivariate analysis based on the bilinear relation (Eq. (1)) is called ‘two-way analysis.’ Recently, the technique has been extended to more general ‘multiway’ analyses [33] or tensor decompositions [34], which will introduce mathematically, sophisticated and flexible techniques to find hidden information embedded in complex datasets. These techniques are being explored for applications in spectral data analysis [35] and are expected to bring new insights in this research field.

Acknowledgments

We are grateful to Drs. T. Sasaki, H. Kondo, K. Horibuchi and T. Ohsuna of Toyota Central R&D Laboratories for supplying LIB cathode material samples as part of our continuous collaboration.

Funding

This work is supported in part by JSPS KAKENHI (Grant-in-Aid for Scientific Research) #25106004 (Innovative Areas "Nano Informatics"), #16H01544 (Innovative Areas “Sparse modelling”), and #26249096 (Kiban-kenkyu A).

References

[1]https://tools.thermofisher.com/content/sfs/brochures/WS52730-Detecting-Lithium-EDS.pdf#search='windowless+EDS+EDX+lithium+Li'

[2] Terauchi M, Takahashi H, Handa N, Murano T, Koike M, Kawachi T, Imazono T, Koeda M, Nagano T, Sasai H, Oue Y, Yonezawa Z and Kuramoto S (2012) Ultrasoft-X-ray emission spectroscopy using a newly designed wavelength-dispersive spectrometer attached to a transmission electron microscope. *J. Electron Microsc.* **61**:

1-8.

[3] Russ J C, Ashby M, Kiessling R and Charles J (1984) *Fundamentals of Energy Dispersive X-ray Analysis*. (Butterworths, London) ISBN: 978-0-408-11031-0.

[4] Shao-Horn Y, Croguennec L, Delmas C, Nelson E C and O'Keefe M A (2003) Atomic resolution of lithium ions in $LiCoO_2$. *Nat. Mater.* **2:** 464.

[5] Chung S-Y, Choi S-Y, Yamamoto T and Ikuhara Y (2008) Atomic-scale visualization of antisite defects in $LiFePO_4$. *Phys. Rev. Lett.* **100**: 125502.

[6] Oshima Y, Sawada H, Hosokawa F, Okunishi E, Kaneyama T, Kondo Y, Niitaka S, Takagi H, Tanishiro Y and Takayanagi K (2010) Direct imaging of lithium atoms in LiV_2O_4 by spherical aberration-corrected electron microscopy. *J. Electron Microsc.* **59**: 457–461.

[7] Egerton R F (1996) *Electron Energy-Loss Spectroscopy in the electron microscope*. (Plenum Press, New York.) p.246, p.269 ISBN: 978-1-4615-6887-2.

[8] Jeanguillaume C and Colliex C (1989) Spectrum-image: The next step in EELS digital acquisition and processing. *Ultramicrosc*. **28**: 252-257.

[9] Kikkawa J, Akita T, Tabuchi M, Shikano M, Tatsumi K and Kohyama M (2008) Real-space observation of Li extraction/insertion in $Li_{1.2}Mn_{0.4}Fe_{0.4}O_2$ positive electrode material for Li-Ion batteries. *Electrochem. Solid-State Lett.* **11:** A183-A186.

[10] Koch C T, Sigle W, Höschen R, Rühle M, Essers E, Benner G and Matijevic M (2006) SESAM: Exploring the frontiers of electron microscopy. *Microsc. Microanal*. **12**: 506-514.

[11] Reimer L, Fromm I and Rennekamp R (1988) Operation modes of electron spectroscopic imaging and electron energy-loss spectroscopy in a transmission electron microscope. *Ultramicrosc*. **24**: 339-354.

[12] Kimoto K, Sekiguchi T and Aoyama T (1997) Chemical shift mapping of Si L and K edges using spatially resolved EELS and energy-filtering TEM. *J. Electron Microsc.* **46**: 369–374.

[13] Yamamoto K, Yoshida R, Sato T, Matsumoto T H, Kurobe H, Hamanaka T, Kato T, Iriyama Y and Hirayama T (2014) Nano-scale simultaneous observation of

Li-concentration profile and Ti-, O electronic structure changes in an all-solid-state Li-ion battery by spatially-resolved electron energy-loss spectroscopy. *J. Power Sources*. **266**: 414-421.

[14] Muto S, Sasano Y, Tatsumi K, Sasaki T, Horibuchi K, Takeuchi Y and Ukyo Y (2009) Capacity-fading mechanisms of $LiNiO_2$-based lithium-ion batteries: II. diagnostic analysis by electron microscopy and spectroscopy. *J. Electrochem. Soc*. **156**: A371-A377.

[15] Honda Y, Muto S, Tatsumi K, Kondo H, Horibuchi K, Kobayashi T and Sasaki T (2015) Microscopic mechanism of path-dependence on charge-discharge history in lithium iron phosphate cathode analysis using scanning transmission electron microscopy and electron energy-loss spectroscopy spectral imaging. *J. Power Sources*. **291**: 85-94.

[16] Muto S, Yoshida T and Tatsumi K (2009) Diagnostic nano-analysis of materials properties by multivariate curve resolution applied to spectrum images by S/TEM-EELS. *Mater. Trans*. **50**: 964-969.

[17] Bonnet N, Brun N and Colliex C (1999) Extracting information from sequences of spatially resolved EELS spectra using multivariate statistical analysis. *Ultramicrosc*. **77**: 97–112.

[18] Trebbia P and Bonnet N (1990) EELS elemental mapping with unconventional methods I. Theoretical basis: Image analysis with multivariate statistics and entropy concepts. *Ultramicrosc.* **34**: 165-178.

[19] Bosman M, Watanabe M, Alexander D T L and Keast V J (2006) Mapping chemical and bonding information using multivariate analysis of electron energy-loss spectrum images. *Ultramicrosc*. **106**: 1024–1032.

[20] Wang J-H, Hopke P K, Hancewicz T M and Zhang S L (2003) Application of modified alternating least squares regression to spectroscopic image analysis. *Anal. Chim. Acta.* **476**: 93-109.

[21] Yoshida T, Muto S, Wakabayashi J (2007) Depth-resolved EELS and chemical state mapping of N^+-implanted TiO_2 photocatalyst. *Mater. Trans.* **48**: 2580–2584.

[22] Kojima Y, Muto S, Tatsumi K, Kondo H, Oka H, Horibuchi K and Ukyob Y (2011) Degradation analysis of a Ni-based layered positive-electrode active material cycled at elevated temperatures studied by scanning transmission electron microscopy and electron energy-loss spectroscopy. *J. Power Sources*. **196**: 7721– 7727.

[23] Berry M W, Browne M, Langville A N, Pauca P and Plemmons R J (2007) Algorithms and applications for approximate nonnegative matrix factorization. *Comput. Stat. Data Anal*. **52**: 155–173.

[24] Shiga M, Tatsumi K, Muto S, Tsuda K, Yamamoto Y, Mori T and Tanji T (2016) Sparse Modeling of EELS and EDX Spectral Imaging Data by Nonnegative Matrix Factorization. To be published in *Ultramicrosc*.

[25] Tan V Y F and Fevotte C (2013) Automatic Relevance Determination in Nonnegative Matrix Factorization with the beta-Divergence. *IEEE Trans. on Pat. Anal. Mach. Intell.* **35**: 1592–1605.

[26] Kimura K, Tanaka Y and Kudo M (2014) A fast hierarchical alternating least squares algorithm for orthogonal nonnegative matrix factorization. *Proc. of the 6th Asian Conference on Machine Learning* 129–141.

[27] Muto S, Tatsumi K, Sasaki, Kondo T H, Ohsuna T, Horibuchi K and Takeuchi Y (2010) Mapping of heterogeneous chemical states of lithium in a $LiNiO_2$-based active material by electron energy-loss spectroscopy. *Electrochem. Solid State Lett.* **13**: A115–A117.

[28] Blaha P, Schwalz K, Madsen G K H, Kvasnicka D and Luitz J (2001) *WIEN2k, An Augmented Plane Wave + Local Orbitals Program for Calculating Crystal Properties.* (Karlheinz Schwarz, Techn. Universität Wien, Austria) ISBN: 3-9501031-1-2.

[29] Olovsson W, Tanaka I, Mizoguchi T, Puschnig P and Ambrosch-Draxl C (2009) All-electron Bethe-Salpeter calculations for shallow-core x-ray absorption near-edge structures. *Phys. Rev. B*. **79**: 041102(R).

[30] Xu M, Xiao A, Li W and Lucht B L (2010) Investigation of lithium tetrafluorooxalatophosphate [$LiPF_4(C_2O_4)$] as a lithium-ion battery electrolyte for elevated temperature performance. *J. Electrochem. Soc*. **157**: A115-A120.

[31] Ramana C V, Ait-Salah A, Utsunomiya S, Morhange J-F, Mauger A, Gendron F and Julien C M (2007) Spectroscopic and chemical imaging analysis of lithium iron triphosphate. *J. Phys. Chem. C.* ***111*** **(2)**: 1049–1054.

[32] Sasaki T, Nonaka T, Oka H, Okuda C, Itou Y, Kondo Y, Takeuchi Y, Ukyo Y, Tatsumi K and Muto S (2009) Capacity-fading mechanisms of $LiNiO_2$-based lithium-ion batteries: I. Analysis by electrochemical and spectroscopic examination. *J. Electrochem. Soc*. **156**: A289-A293.

[33] Smilde A, Bro R, and Geladi P (2004) *Multiway Analysis with Applications in the Chemical Sciences*. (John Wiley, Chichester) ISBN: 978-0-471-98691-1.

[34] Cichocki A, Mandic D, Phan A-H, Caiafa C, Zhou G, Zhao Q, and De Lathauwer L (2015) Tensor decompositions for signal processing applications. *IEEE Signal Processing Magazine* **32:** 145-167.

[35] Spiegelberg J, Rusz J, and Pelckmans K (2016) Tensor decompositions for the analysis of electron energy loss spectroscopy data. *Ultramicros*c. to be published.

Figure captions

Fig. 1 Three different modes for obtaining a spectral image dataset. (a) STEM-EELS, (b) Energy filtered-TEM (EF-TEM) and (c) Spatially resolved-EELS (SR-EELS) for cross sectional TEM (XTEM) observation of multi-layer samples.

Fig. 2 ELNES spectra of LiF and several representative transition metal compounds in the range of 40-80 eV.

Fig. 3 Experimental ELNES spectra of lithium compounds and representative LIB cathode materials in the range of 50-80 eV.

Fig. 4(a) Schematic showing the data structure of SI in Eq. (1), and (b) Schematic representing Eq. (2).

Fig. 5(a) ADF-STEM image of NCA cathode active particle before cycling. The framed area was scanned for SI. (b) Extracted ELNES from the entire framed area in (a). Expected spectrum onset is indicated for each element contained. (c) Energy-filtered image constructed by setting the energy slit to pick up the first distinct peak in (b). (d) Extracted ELNES spectra from spots #1 and #2 indicated in (a).

Fig. 6 Results of NMF decomposition showing spatial distributions of (a) component #1 and (b) component #2. The pure component spectra are shown in (c). The blue broken lines in the graph represent the main peak positions of component #2.

Fig. 7 Theoretically simulated Li–K ELNES spectrum (black solid line) for $Li_xPO_yF_z$. The spectrum consists of two distinct peaks from the two local atomic configurations, as indicated by the red and the blue lines in the figure. The blue broken lines correspond to the positions of those in Fig. 6(c).

Fig. 8(a) ADF-STEM image of NCA cathode active particles after 500 cycles at 70 °C. (b) and (c) Spatial distribution maps of the extracted spectral components, and (d) Spectra of pure component #1 and #2, resolved by NMF. The blue broken lines correspond to the characteristic peak positions shown in Fig. 9.

Fig. 9 Theoretical Li K ELNES spectrum of Li substituted at a Ni site in NiO (red line), and Li in $LiNiO_2$ (black line) for the energy axis calibration. The blue broken lines mark the characteristic peak positions.

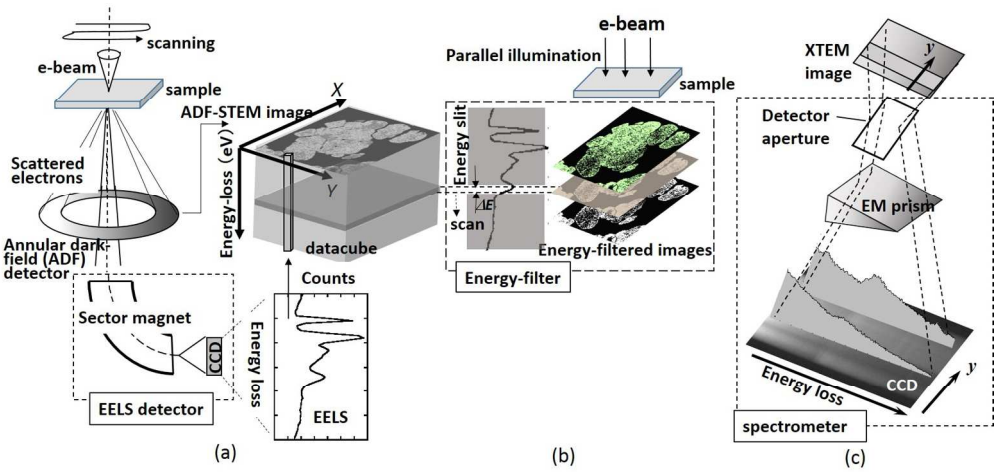

301x144mm (150 x 150 DPI)

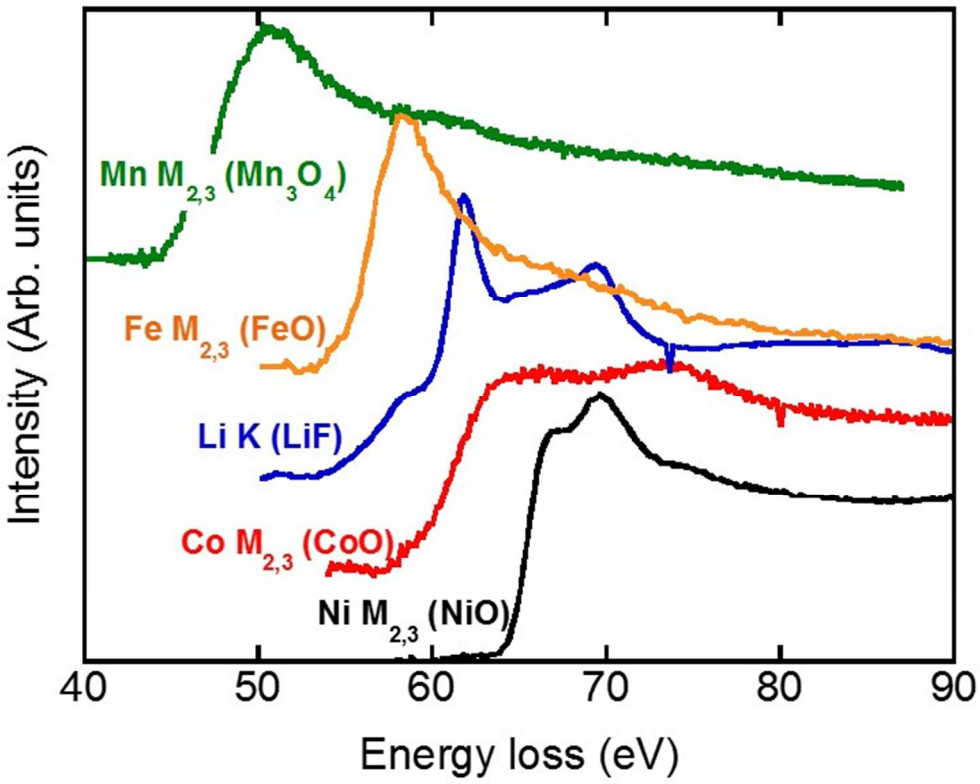

Fig. 2 ELNES spectra of LiF and several representative transition metal compounds in the range of 40-80 eV.
Fig. 2
259x204mm (72 x 72 DPI)

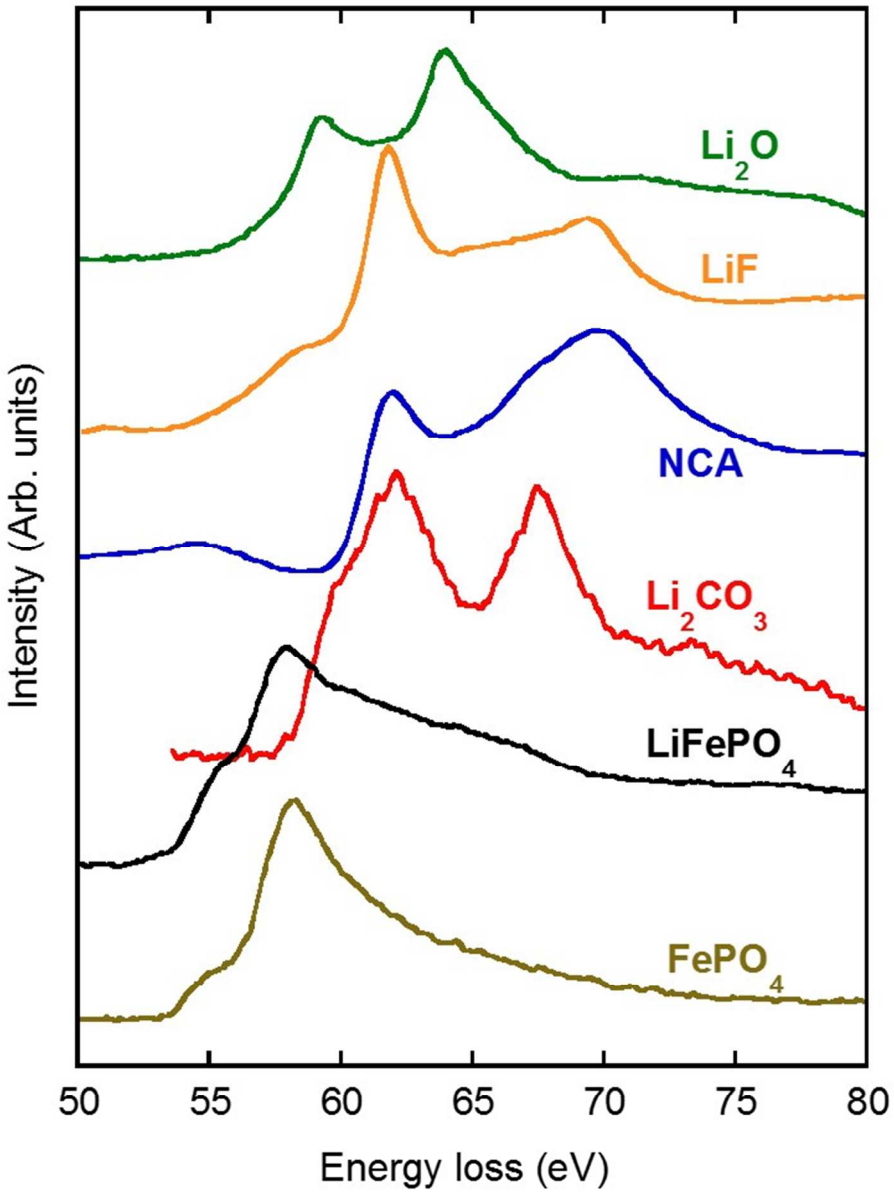

Fig. 3 Experimental ELNES spectra of lithium compounds and representative LIB cathode materials in the range of 50-80 eV.
Fig. 3
259x341mm (72 x 72 DPI)

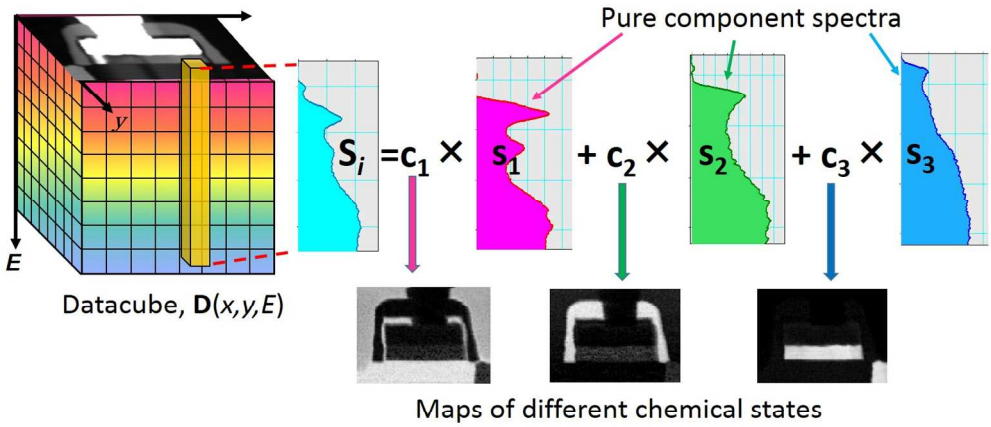

(a)

Fig. 4(a) Schematic showing the data structure of SI in Eq. (1) and (b) Schematic representing Eq. (2).
Fig. 4a
584x308mm (72 x 72 DPI)

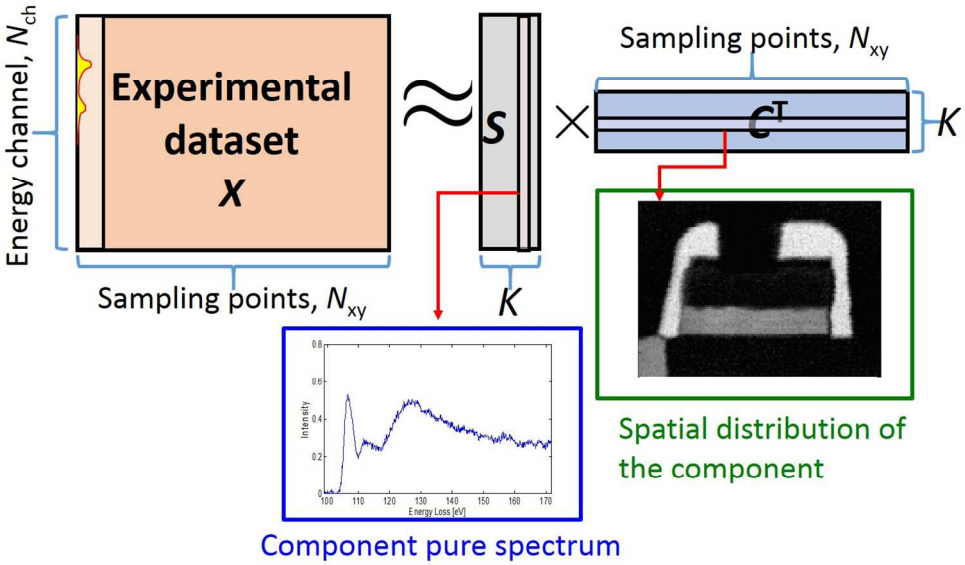

(b)

Fig.4b
535x370mm (72 x 72 DPI)

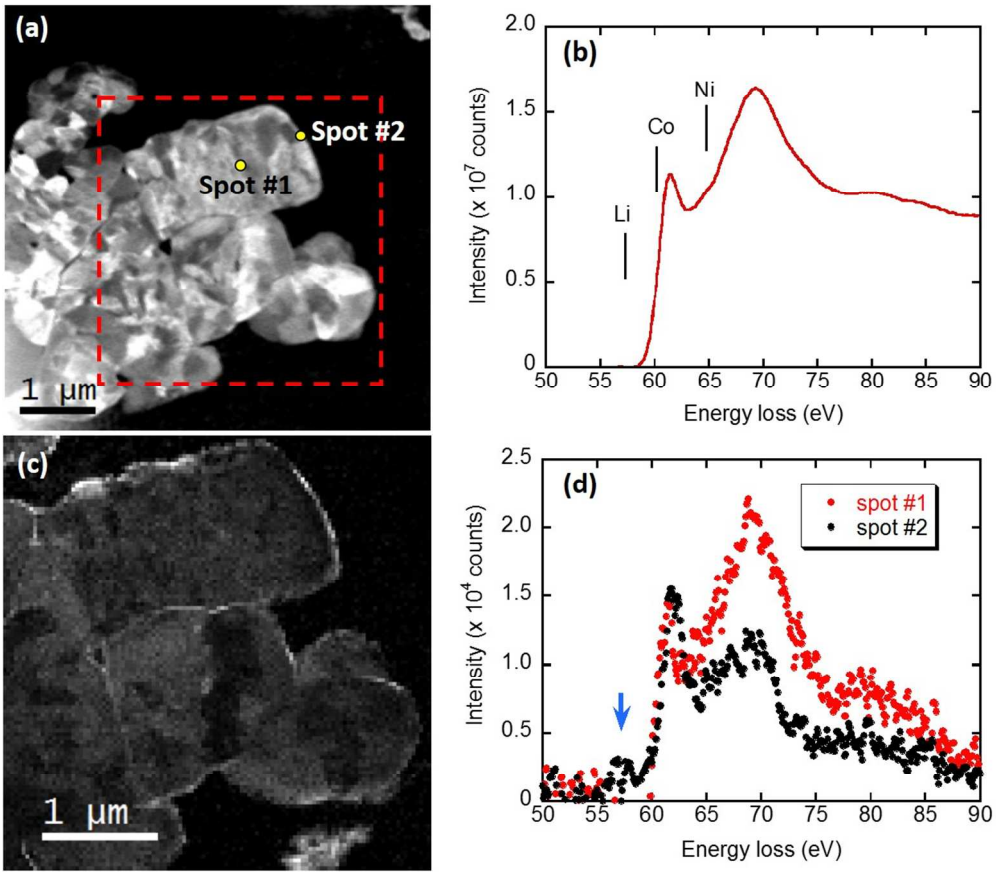

Fig. 5(a) ADF-STEM image of NCA cathode active particle before cycling. The framed area was scanned for SI, (b) Extracted ELNES from the entire framed area in (a). Expected spectrum onset is indicated for each element contained, (c) Energy-filtered image constructed by setting the energy slit to pick up the first distinct peak in (b), (d) Extracted ELNES spectra from spots #1 and #2 indicated in (a).
Fig. 5
439x383mm (72 x 72 DPI)

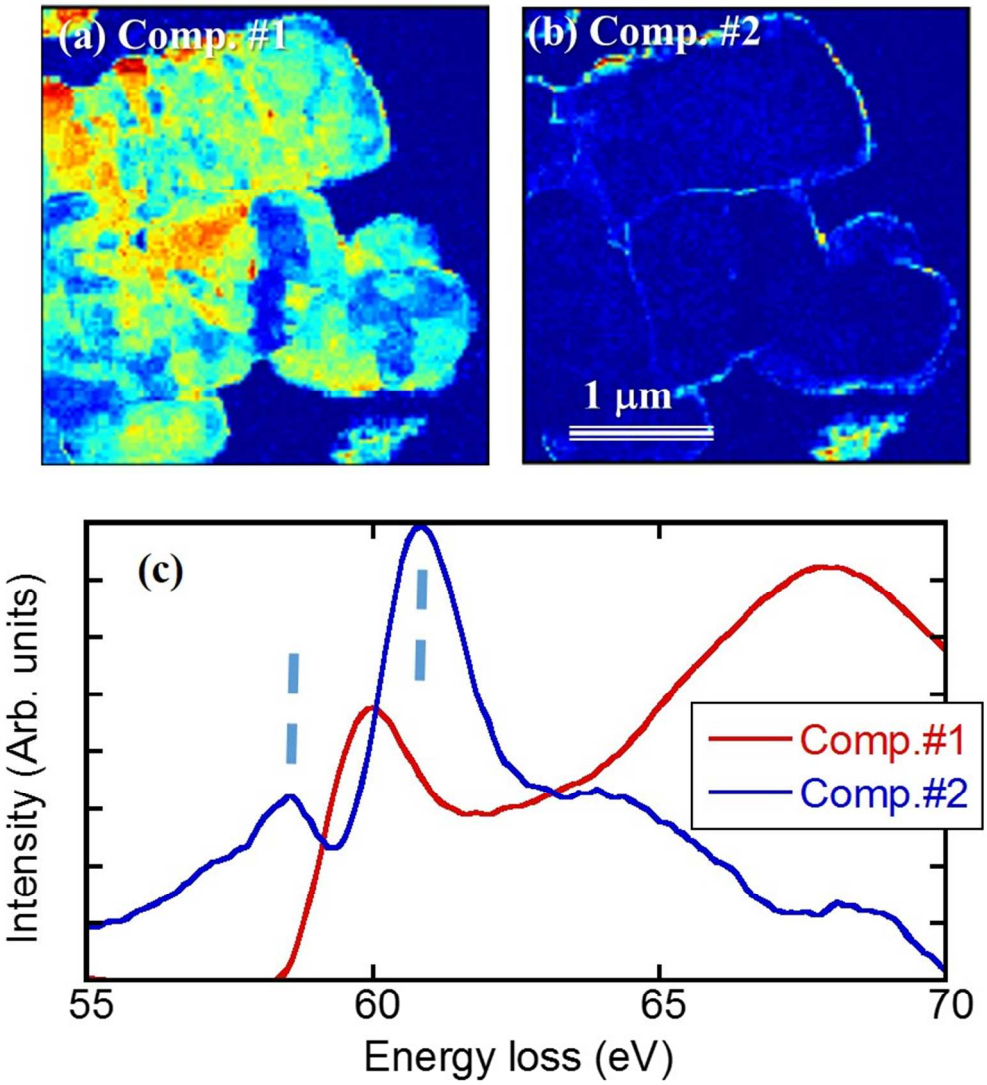

Fig. 6 Results of NMF decomposition showing spatial distributions of (a) component #1 and (b) component #2. The pure component spectra are shown in (c). The blue broken lines in the graph represent the main peak positions of component #2.
Fig. 6
316x348mm (72 x 72 DPI)

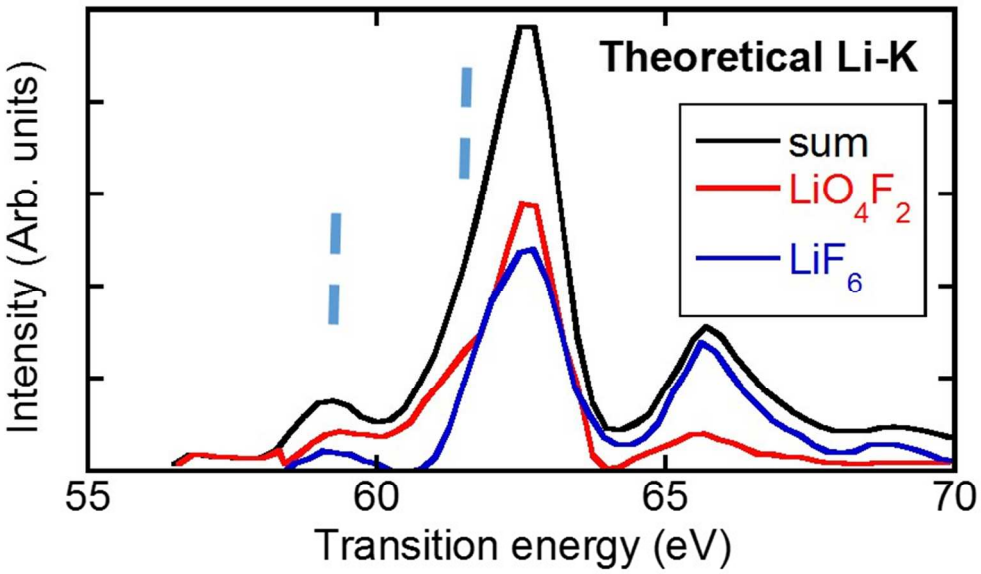

Fig. 7 Theoretically simulated Li–K ELNES spectrum (black solid line) for LixPOyFz. The spectrum consists of two distinct peaks from the two local atomic configurations, as shown by red and blue lines in the figure. The blue broken lines correspond to the positions of those in Fig. 6(c).
Fig. 7
313x182mm (72 x 72 DPI)

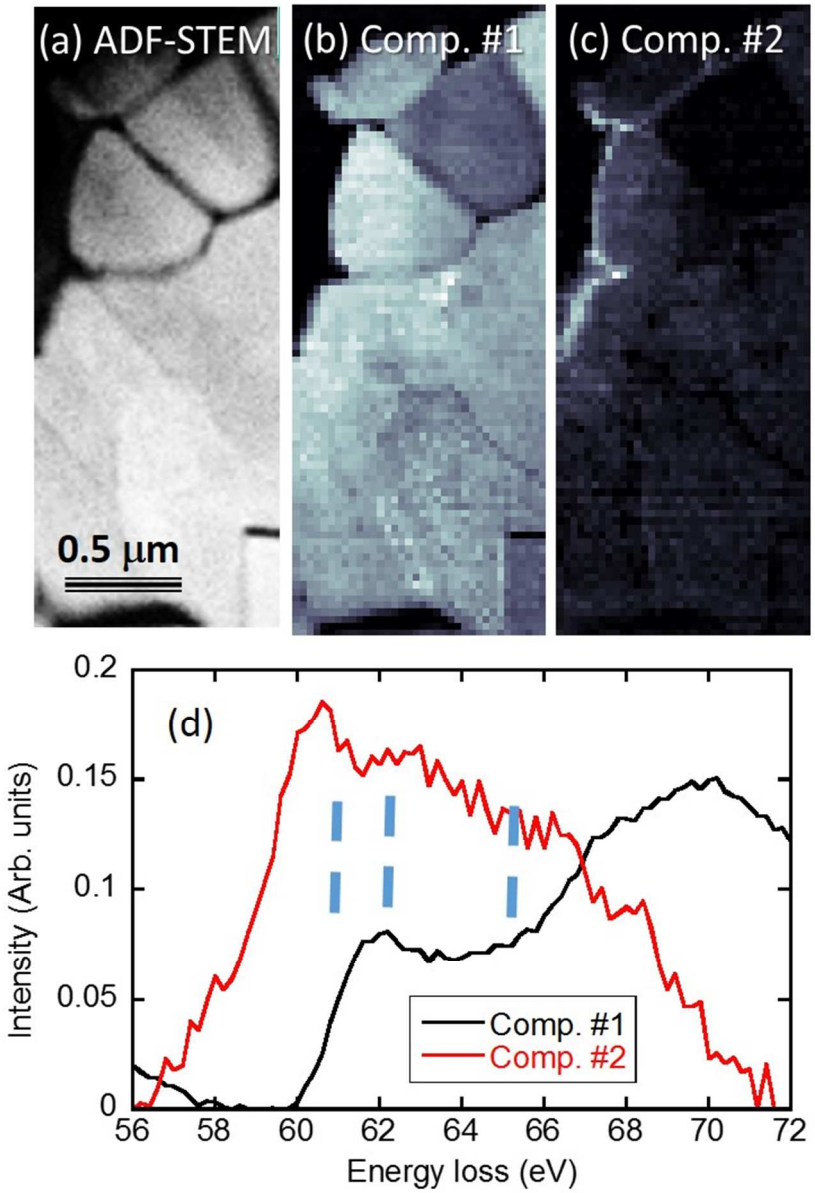

Fig. 8(a) ADF-STEM image of NCA cathode active particles after 500 cycles at 70 °C. (b) and (c) Spatial distribution maps of the extracted spectral components and (d) Spectra of pure component #1 and #2, resolved by NMF. The blue broken lines correspond to the characteristic peak positions shown in Fig. 9.

Fig. 8

257x376mm (72 x 72 DPI)

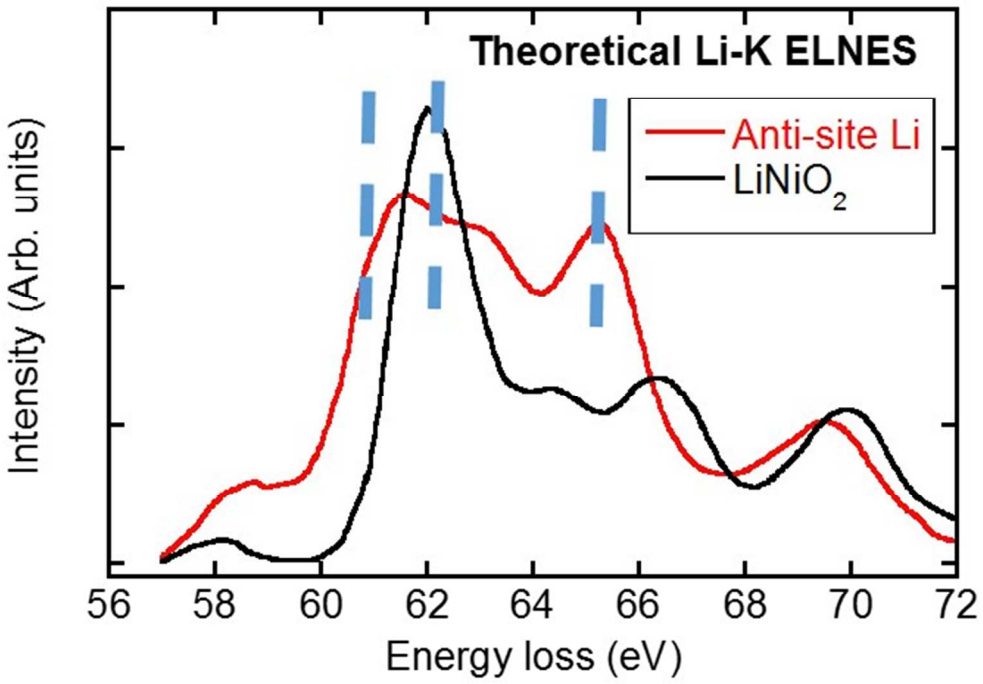

Fig. 9 Theoretical Li K ELNES spectrum of Li substituted at a Ni site in NiO (red line), and Li in LiNiO2 (black line) for the energy axis calibration. The blue broken lines mark the characteristic peak positions.
Fig. 9
239x165mm (72 x 72 DPI)